

# Disorder-induced ordering in gallium oxide polymorphs

Alexander Azarov<sup>1, a)</sup>, Calliope Bazioti<sup>1</sup>, Vishnukanthan Venkatachalamapathy<sup>1,2</sup>,  
Ponniah Vajeeston<sup>3</sup>, Edouard Monakhov<sup>1</sup>, and Andrej Kuznetsov<sup>1, b)</sup>

<sup>1)</sup> *University of Oslo, Department of Physics, Centre for Materials Science and Nanotechnology, PO Box 1048 Blindern, N-0316 Oslo, Norway*

<sup>2)</sup> *Department of Materials Science, National Research Nuclear University, “MEPhI”, 31 Kashirskoe Hwy, 115409 Moscow, Russian Federation*

<sup>3)</sup> *University of Oslo, Department of Chemistry, Centre for Materials Science and Nanotechnology, PO Box 1033 Blindern, N-0315 Oslo, Norway*

Polymorphs are common in nature and can be stabilized by applying external pressure in materials. The pressure/strain can also be induced by the gradually accumulated radiation disorder. However, in semiconductors, the radiation disorder accumulation typically results in the amorphization instead of engaging polymorphism. By studying these phenomena in gallium oxide we found that the amorphization may be prominently suppressed by the monoclinic to orthorhombic phase transition. Utilizing this discovery, we fabricated a highly oriented single-phase orthorhombic film on the top of the monoclinic gallium oxide substrate. Exploring this system, we observed a novel mode of a lateral polymorphic regrowth not previously observed in solids. In combination, these data envisage a new direction of research on polymorphs in  $\text{Ga}_2\text{O}_3$  and, potentially, for similar polymorphic families in other materials.

<sup>a)</sup> [alexander.azarov@smn.uio.no](mailto:alexander.azarov@smn.uio.no)

<sup>b)</sup> [andrej.kuznetsov@fys.uio.no](mailto:andrej.kuznetsov@fys.uio.no)

The phenomenon of phase transitions is generic, belonging to the natural science and social science disciplines alike. In material science, the understanding of phase transitions and control over the phase transformations is foundational for the technology development. Indeed, even assuming no chemical reactions or long-range atomic transport to occur, there are still endless examples of polymorphism in crystals [1]. The basic principles of polymorphism in crystals are clear: the lattices adapt to the minimum energy in respect with the temperature and pressure. Meanwhile, controllable stabilization of the metastable phases, e.g. at room temperature, is of great interest because it opts for new properties; however, preferably without applying colossal external pressures [2]. For that matter, reaching metastable conditions via ion beam assisted processes with displaced atoms provoking strain accumulation is an interesting alternative. However, the irradiation-induced disorder may also result in the amorphization instead of engaging the polymorphism, as it occurs in semiconductors, e.g. Si [3] or SiC [4]. Notably, even for so-called “radiation hard” semiconductors, e.g. GaN [5] or ZnO [6], the radiation induced defect accumulation still ends up with high disorder level or partial amorphization.

Thus, in spite that the ion irradiation is known to stimulate the formation of new phases [7], the ion beam induced polymorphism is rarely observed in solids, at least as it holds to semiconductors. Nevertheless, very recently Ander *et al.* have detected  $\kappa$ -phase  $\text{Ga}_2\text{O}_3$  in the  $\beta$ -phase  $\text{Ga}_2\text{O}_3$  matrix formed in the ion implanted samples [8], even though the evolution of this process as a function of the implantation parameters has not been explored. Since  $\text{Ga}_2\text{O}_3$  is well known for its polymorphism [9], we undertook a systematic study of the ion beam induced phase transformation phenomena in  $\text{Ga}_2\text{O}_3$ . By testing a wide range of parameters, we show that the radiation disorder accumulated in the monoclinic  $\beta$ - $\text{Ga}_2\text{O}_3$  indeed assists its transformation into the orthorhombic  $\kappa$ -phase. As such the amorphization is paradoxically avoided by the disorder-induced new phase

ordering. Importantly, we demonstrate a controllable ion-beam-induced phase engineering resulting in the formation of the highly oriented single-phase continuous  $\kappa$ -phase film on the top of the  $\beta$ - $\text{Ga}_2\text{O}_3$  wafer. This result opens for an opportunity to exploit the metastable polymorph films and regularly shaped interfaces in device components not achievable by conventional thin film deposition methods. Thus, the present exploration, in addition to its fundamental value, may accelerate the technological development of  $\text{Ga}_2\text{O}_3$ , which is one of the most intensively studied ultra wide band gap semiconductor right now [10].

Fig.1 summarizes the data proving the ion-beam-induced  $\beta$ -to- $\kappa$  phase transformation in  $\text{Ga}_2\text{O}_3$  combining (a) x-ray diffraction (XRD), (b) Rutherford backscattering spectrometry with channeling (RBS/C), and (c) scanning transmission electron microscopy (STEM) measurements of (010)  $\beta$ - $\text{Ga}_2\text{O}_3$  samples irradiated with  $^{58}\text{Ni}^+$  ions. As it is clearly seen from Fig. 1(a) the virgin  $\beta$ - $\text{Ga}_2\text{O}_3$  wafer is characterized by a strong reflection around  $60.9^\circ$  attributed to the (020) planes of  $\beta$ - $\text{Ga}_2\text{O}_3$ . The low dose implants ( $6 \times 10^{13}$  and  $2 \times 10^{14}$   $\text{Ni}/\text{cm}^2$ ) result in the formation of the shoulder peak with some oscillations at the high-angle side of the (020) peak. These shoulder peak/oscillations can be attributed to the accumulation of the compressive strain as discussed in literature [11]. However, further dose increase ( $1 \times 10^{15}$   $\text{Ni}/\text{cm}^2$ ) releases this strain and leads to the formation of the broad diffraction peak around  $63.4^\circ$ , which shifts to  $63.7^\circ$  for the dose of  $1 \times 10^{16}$   $\text{Ni}/\text{cm}^2$ . Importantly, for this highest dose, the strain shoulder peaks practically disappear and the (020) diffraction peak resembles that in the virgin sample. The diffraction peaks centered at  $63.4^\circ$  and  $63.7^\circ$  were interpreted as signatures of the  $\kappa$ - $\text{Ga}_2\text{O}_3$  (330) and (060) planes, respectively [12], as systematically analyzed in Fig.S1 in Supplementary Materials-I; notably, Fig.S2 illustrates the evolution in the similarly implanted (-201)  $\beta$ - $\text{Ga}_2\text{O}_3$  samples for comparison.

Thus, already the data in Fig.1(a) suggest an interesting scenario for the phase transformation in  $\text{Ga}_2\text{O}_3$  induced by ion irradiation. However, there are remaining questions, e.g. concerning the mechanisms of the transformation and the integrity of the new phase. To answer these questions we applied RBS/C to measure the kinetics of the lattice disorder buildup as shown in Fig.1(b). For the lowest dose sample, the RBS/C spectrum is characterized by the well resolved Gaussian-like damage peak centered close to the maximum of the nuclear energy loss profile ( $R_{pd}=125$  nm according to the SRIM simulations [13]). The magnitude of this peak is well below the amorphous level that is equivalent to the height of the random spectrum in Fig.1(b). The increase of the ion dose up to  $2 \times 10^{14} \text{ cm}^{-2}$  results in the formation of the box-shape disorder layer reaching  $\sim 90\%$  of the random signal. Up to this stage the RBS/C data for  $\beta\text{-Ga}_2\text{O}_3$  resembles the data for other semiconductors [3-6] and as well as for  $\beta\text{-Ga}_2\text{O}_3$  as measured by RBS/C [14]. Further dose increase, to  $1 \times 10^{15} \text{ Ni/cm}^2$ , broadens the disordered layer and the disorder level saturates. Spectacularly, the de-channeling decreases upon collecting the dose of  $1 \times 10^{16} \text{ Ni/cm}^2$ , implying the lattice ordering along the [010] direction, in agreement with the XRD data revealing (060)  $\kappa$ -phase diffraction peak. Thus, even though the radiation disorder reconstruction at high doses was observed in semiconductors before, e.g. [15], in combination, the XRD and RBS/C data in Figs.1(a) and 1(b) are radically novel and support the scenario of the radiation-induced  $\beta$ -to- $\kappa$  phase transformation of the top  $\sim 300$  nm film in the  $1 \times 10^{16} \text{ Ni/cm}^2$  implanted sample. Notably, the de-channeling yield in this sample is still rather high; indicating either a collective tilt between  $\beta$ - and  $\kappa$ -phase [010] directions or mis-orientation between individual crystallites. To verify the status of this film we performed STEM investigations.

Fig. 1(c-h) summarizes the STEM data for the sample implanted with  $1 \times 10^{16}$  Ni/cm<sup>2</sup>. Specifically, Fig.1(c) shows an Annular Bright Field (ABF)-STEM image and strain contrast reveals the formation of two distinct regions – the film and the substrate – of the initially homogeneous  $\beta$ -Ga<sub>2</sub>O<sub>3</sub> wafer. Selected area electron diffraction (SAED) patterns taken from the unimplanted and implanted regions, i.e. Figs.1(d) and 1(e), illustrate a prominent transformation from monoclinic  $\beta$ - to ordered orthorhombic  $\kappa$ -phase. This phase transformation extends to  $\sim 300$  nm from the surface and stops abruptly, forming a sharp interface with the  $\beta$ -phase wafer/substrate, see Fig.1(c). The contrast associated with defects/strain inside the  $\kappa$ -Ga<sub>2</sub>O<sub>3</sub> film gradually increases towards the  $\kappa$ - $\beta$  interface, see Fig.1(c). However, fast Fourier transforms (FFTs) from high-resolution images taken at the interfacial area (g) and the upper part (h) of the implanted region show that the ordered orthorhombic phase is retained through the depth of the film as compared with the FFT at the  $\beta$ -Ga<sub>2</sub>O<sub>3</sub> substrate, see Fig.1(f). Thus, SAED and FFTs show the formation of a single-phase ordered orthorhombic  $\kappa$ -phase region both at meso and nano-scale. The sharp spots, in addition to the lack of extra reflections and/or striking of the main reflections, indicate a highly-oriented crystalline film with no signs of high-angle mis-orientations, high-density of mis-oriented grains or amorphization (see also Fig.S3 in Supplementary Materials II). However, minor mis-orientations between adjacent grains cannot be excluded, playing a role in the high de-channeling yield in RBS/C and the broadening of the XRD peaks in Fig.1.

To obtain further insights into this interesting process, Fig.2 shows the STEM analysis of the sample implanted with  $6 \times 10^{13}$  Ni/cm<sup>2</sup> in panels (a-d) and its comparison with the  $1 \times 10^{16}$  Ni/cm<sup>2</sup> sample in terms of the electron energy loss spectroscopy (EELS) spectra in panel (e). The (ADF)-STEM image reveals that the strain contrast in the implanted region gradually reduces when moving away from the  $R_{pd}$ , with no signs of abrupt changes, see

Fig.2(a). This region is likely to contain point defects and defect clusters, but no amorphous areas were detected in the entire implanted region. This is confirmed by a combination of the SAED and FFT in Figs.2(b-d). Thus,  $\beta$ -phase is identified through all regions in Fig.2(a) with no signs of phase transitions; meanwhile the accumulation of strain is confirmed in this sample. Moreover, the comparison between EELS spectra in Fig.2(e) provides additional arguments. Indeed, because of different atomic coordination in  $\beta$ - and  $\kappa$ -phases we detected characteristic changes in the fine structure of the EELS spectra acquired in STEM-mode, by comparing low and high-dose implanted samples. In particular, the oxygen-K-edge is characterized by two main peaks, labelled A and B in Fig.2(e), related to the O 2p - Ga 4s and O 2p - Ga 4p bonding, respectively. As seen from Fig.2(e), prominent changes in the A/B intensity ratio ( $I_A/I_B$ ) occur when the phase transition takes place. Specifically,  $I_A/I_B$  decreases in the  $\kappa$ -phase. This can be attributed either to the increase in O 2p – Ga 4p hybridization or to the transfer of electrons from O 2p – Ga 4p band into another band [8, 16].

At this stage, we conclude that Figs.1 and 2 comprise a new fundamental observation - least as it holds for semiconductors - prominent suppression of the amorphization by the  $\beta$ -to- $\kappa$  phase transition in  $\text{Ga}_2\text{O}_3$ . It is remarkable that the accumulated lattice disorder results in the ordering of the single-phase film without inclusions of the secondary phase and exhibiting high crystalline quality. Moreover, the regular interfaces of the polymorph film, similar to  $\beta/\kappa$  interface in Fig.1(c), to the best of our knowledge, were not demonstrated in the literature before. Possibly, the ion-beam synthesis of metastable polymorphs is the only practical method to fabricate such films/interfaces not achievable by conventional thin film deposition methods; because of the practical difficulty to maintain the required level of strain over the desired area/volume of the material. Thus, to

put our fundamental discovery into the perspective of potential applications, we investigated the properties of these polymorph films in further details.

Firstly, we considered the preferential orientation(s) of the  $\kappa$ -phase films synthesized in the present work. As mentioned earlier, we identified the peak centered at  $63.7^\circ$  as the (060) plane reflection in  $\kappa\text{-Ga}_2\text{O}_3$ . We attribute the broadness of this (060) peak to the residual strain remaining in the  $\kappa\text{-Ga}_2\text{O}_3$  film and specifically to different strain levels at different depth of the film, all contributing into the XRD signal; additionally, the broadness can be attributed to minor mis-orientations of the adjacent grains too. Interestingly, the preferential orientation of the  $\kappa$ -phase film may change in the course of the dose accumulation. For example, the  $63.4^\circ$  peak in Fig.1(a) is attributed to (330) planes; consistently with the de-channeling yield variations in Fig.1(b). Moreover, as also shown in Fig.S2 in Supplementary Materials-I, the implants into (-201)  $\beta\text{-Ga}_2\text{O}_3$  samples unveil similar process of the strain accumulation and phase transition, however visualized with other crystal planes detectable by XRD in these samples. Altogether, it suggests a very interesting balance for the  $\beta$ -to- $\kappa$  phase transformation as a function of the radiation induced lattice disorder in respect with the anisotropy of the strain acting along different crystallographic directions.

Secondly, we emphasize that the phenomenon of the  $\beta$ -to- $\kappa$  phase transition observed in Figs.1 and 2 is generically related to the accumulation of the lattice disorder and not to the chemical nature of the implanted ions. This was proved by performing control implants with Ga and Au ions to the doses corresponding to the same number of primary defects as that generated by Ni ions (see Figs.S1 and S4 in the Supplementary Materials I and III). Moreover, STEM analysis reveals no chemical interactions, as such confirming negligible

roles of the chemical effects associated with implanted ions used in the present work (Ni, Ga, Au) on the phase transformations in the  $\text{Ga}_2\text{O}_3$  matrix, even at the atomic-scale.

Thirdly, we investigated the temperature stability of the  $\kappa$ - $\text{Ga}_2\text{O}_3$  film from Fig.1(c). The evolution – see Fig.3 – is indeed very interesting. The RBS/C data show that the anneals at 300-700 °C result in the reduction of the  $\kappa$ -film thickness as revealed by the shifts of the RBS/C spectra in the range corresponding to the  $\beta/\kappa$  interface region. However, increasing the temperature to 700 °C enhances the de-channeling, in particular in the near surface region, indicating the disintegration of the  $\kappa$ -phase film. The corresponding XRD data in Fig.3(b) show that the central position of the (060)  $\kappa$ -phase peak moves too. In fact for 300-500 °C it moves towards better fits with literature data [12]. This shift may indicate an improvement of the  $\kappa$ - $\text{Ga}_2\text{O}_3$  phase crystallinity because of annealing of the misoriented grains at the  $\beta/\kappa$  interface region consistently with the RBS/C data in Fig.3(a).

Thus, based on the data in Fig.3, we can emphasize an interesting observation, not yet reported in literature: lateral solid-phase regrowth of the polymorphs. The kinetics of this process resembles that of the solid phase epitaxial regrowth of the amorphous phase induced by ion irradiation, e.g. for amorphous silicon [3], even though in reality Fig.3 reveals the crystalline phase transition. The inset in Fig. 3(a) plots the rate of this process as a function of the annealing temperature, revealing the activation energy of  $0.16 \pm 0.1$  eV. Notably, in accordance with literature [17]  $\kappa$ - $\text{Ga}_2\text{O}_3$  deposited with conventional techniques starts to degrade at  $\sim 650$  °C, but the nucleation of the  $\beta$ -phase occurs in the bulk of the  $\kappa$ -phase layer. Thus, our results suggest an important role of the  $\beta/\kappa$  interface for the thermal stability of radiation induced  $\kappa$ - $\text{Ga}_2\text{O}_3$  films. The detailed investigations of the  $\beta/\kappa$  lateral front advance have be done in future, but already our data confirm that there is a tilt at the interface between [010]  $\beta$ - and  $\kappa$ -phases. Indeed, during STEM, the sample

has to be tilted separately to bring each phase to the zone axis, in particular meaning that the SAED patterns in Fig.1 were recorded at different tilts.

The fundamental reason of the  $\kappa$ -phase metastability is of a thermodynamic origin and we analyzed  $\text{Ga}_2\text{O}_3$  phases using the density functional theory (DFT). We illustrate the major conclusions of this analysis with Fig.4, while the details are available from the Supplementary Materials-IV. Indeed, Fig.4 shows the total energy for  $\alpha$ -,  $\beta$ -, and  $\kappa$ - $\text{Ga}_2\text{O}_3$  lattices subjected to isotropic or uniaxial pressure, plotted as a function of volume per formula unit (f.u.) for two different intervals in panels (a) and (b). Notably, there are more  $\text{Ga}_2\text{O}_3$  polymorphs available, however  $\alpha$ -,  $\beta$ -, and  $\kappa$ -phases are the lowest in energy as seen from Fig.S5 in Supplementary Materials-IV. In particular, the  $\kappa$ -phase exhibits its energy minimum closest to that of  $\beta$ -phase, making the  $\beta$ -to- $\kappa$  transition likely to occur as soon as sufficient strain is provided ( $\sim 2\%$ , corresponding to the volume of  $\sim 51.35 \text{ \AA}^3/\text{f.u.}$  in Fig.4 for isotropic pressure/strain). Thus, we believe that such strain conditions are gradually reached by the implants in Figs.1(a) and (b), finally resulting in the  $\kappa$ -phase film as shown in Fig.1(c). Meanwhile, the strain sufficient to ignite  $\beta$ -to- $\alpha$  phase transition is only slightly higher, see Fig.4(a); meaning that the formation of the  $\alpha$ -phase is also possible, as was also experimentally demonstrated under high isotropic pressure [18]. To start this process, there is an additional activation volume to overcome (as compared to  $\beta$ -to- $\kappa$  transition), since the energy minima for the  $\alpha$ -phase corresponds to the volume of  $\sim 50.5 \text{ \AA}^3/\text{f.u.}$  in Fig.4(a). This explains the reason of the single-phase  $\kappa$ -film in Fig.1(c) instead of the  $\alpha/\kappa$ -phase mixture or  $\alpha$ -phase alone. Thus, the scenario behind the observations in Figs.1 and 2 is consistent the theoretical predictions of the radiation disorder-induced strain reaching a threshold to ignite the  $\beta$ -to- $\kappa$  transition and, consequently, relaxing the strain by moving the system to the  $\kappa$ -phase energy minimum in Fig.4(a).

Notably, Fig.4 also compares the isotropic and uniaxial pressures, since at present we do not have sufficient experimental arguments to conclude on the strain distribution. Non-isotropic strain conditions are realistic because of the preferential localizations of the radiation defects and building defect complexes with specific configurations [19], likely compressing/stretching certain crystal directions. Nevertheless, for the pressures applied, non-negligible energy difference, as compared with the isotropic strain, occurs in  $\kappa$ -Ga<sub>2</sub>O<sub>3</sub> only, see Fig.4(b). Interestingly, it shifts the  $\kappa$ -Ga<sub>2</sub>O<sub>3</sub> energy curve towards the “triple point” intersection for  $\alpha$ ,  $\beta$ , and  $\kappa$ -phases at the volume of  $\sim$ 51.2 Å<sup>3</sup>/f.u. in Fig.4(b). Additional important parameter not taken into account in Fig.4 is temperature. Indeed, the data in Fig.4 represent the ground state only, while the temperature shifts the stability range for all phases as illustrated in Fig.S8 in Supplementary Materials-IV. Moreover, temperature might affect the balance between out-diffusion and annihilation of the radiation-induced defects [11], making it to an important factor for the localization of the  $\beta/\kappa$  interface in respect with the  $R_{pd}$  region (see Fig.S9 in Supplementary Materials –V).

Thus, the interplay between the lattice disorder accumulation, strain (including its potential anisotropy), and temperature are the factors to be explored in the future studies in order to develop reliable Ga<sub>2</sub>O<sub>3</sub> polymorph fabrication with ion beams, not least with the emphasis on the functional properties of the films. Notably, this fabrication method may potentially help to design even not yet thinkable device components containing sharp polymorph interfaces, e.g. using combinations of conventional and focused ion beams. As such, the present discovery, in addition to its fundamental value, may accelerate the technological development of gallium oxide, which is one of the most intensively studied ultra wide band gap semiconductors right now [10].

In conclusion, we have observed and explained highly ordered, well-defined polymorphic phase transition in ion implanted  $\text{Ga}_2\text{O}_3$ . The mechanism involves the lattice disorder-induced strain accumulation that ignites the transition upon reaching sufficient strain threshold as predicted by theory. Utilizing this discovery, we fabricated a [010] oriented single phase orthorhombic  $\kappa$ -phase film on the top of the [010] oriented monoclinic  $\beta$ -phase substrate, demonstrating sharp  $\kappa/\beta$  interface not previously realized by conventional thin film deposition methods. We also observed a novel mode of solid-phase polymorphic regrowth of  $\beta$ -phase on the expense of  $\kappa$ -phase film spectacularly maintained across the lateral  $\kappa/\beta$  interface and exhibiting the activation energy of  $0.16\pm0.1$  eV at  $300\text{-}500^\circ\text{C}$ . In combination, the present work paves the way for further development of the polymorph films and interfaces by ion beam fabrication, envisaging this new research direction for  $\text{Ga}_2\text{O}_3$  and, potentially, for similar polymorphic families in other materials.

## ACKNOWLEDGMENTS

This work was performed within the Research Centre for Sustainable Solar Cell Technology (FME SuSolTech, project number 257639) and co-sponsored by the Research Council of Norway and industry partners. The Research Council of Norway is acknowledged for the support to the Norwegian Micro- and Nano-Fabrication Facility, NorFab, project number 295864, and to the Norwegian Center for Transmission Electron Microscopy, NORTEM, project number 197405/F50. We also acknowledge the Research Council of Norway for providing the computer time, project numbers NN2875k and NS2875k) at the Norwegian Supercomputer Facility. The INTPART Program at the Research Council of Norway, project number 261574, enabled the international collaboration.

## Methods

## Samples and implants

We used (010) and (-201) oriented  $\beta$ -Ga<sub>2</sub>O<sub>3</sub> single crystal wafers purchased from the Tamura Corp. The wafers were laser cut into 5×5 mm samples used for the implants. The implants were performed at room temperature with different ions, specifically <sup>58</sup>Ni<sup>+</sup>, <sup>69</sup>Ga<sup>+</sup>, and <sup>197</sup>Au<sup>+</sup>. In the present paper most of the data are shown for systematic <sup>58</sup>Ni<sup>+</sup> ion implants, while <sup>69</sup>Ga<sup>+</sup>, and <sup>197</sup>Au<sup>+</sup> implants data are used for comparison to demonstrate the general character of the phenomena. For that reason, the ballistic defect production rates (without accounting for non-linear cascade density effects [20]) for <sup>69</sup>Ga<sup>+</sup>, and <sup>197</sup>Au<sup>+</sup> implants were normalized to that of <sup>58</sup>Ni<sup>+</sup> ion implanted with 400 keV in a wide dose range of  $6\times10^{13}$  -  $1\times10^{16}$  cm<sup>-2</sup>. For <sup>58</sup>Ni<sup>+</sup> implants the ion flux was kept constant at  $\sim4\times10^{12}$  at/(cm<sup>2</sup>s) to enable systematic comparison, as we recently confirmed that the dose-rate effect plays a significant role in the disorder accumulation in  $\beta$ -Ga<sub>2</sub>O<sub>3</sub> [11]. The implantations were performed maintaining 7° off-angle orientation from normal direction to minimize channeling.

## Characterization

The samples were analyzed by a combination of Rutherford backscattering spectrometry in channeling mode (RBS/C), x-ray diffraction (XRD) and scanning transmission electron microscopy (STEM) combined with electron energy loss spectroscopy (EELS). The RBS/C was performed using 1.6 MeV He<sup>+</sup> ions incident along [010] direction and backscattered into a detector placed at 165° relative the incident beam direction. RBS/C is a powerful technique for analysis of ion-induced disorder as well as crystalline quality of the materials [21]. Since the (010) oriented samples demonstrated the best channeling and, therefore, provided better accuracy in the disorder accumulation measurements, we used these data for systematic analysis in the present paper, while the data for (-201) samples are shown for comparison only. Notably, even though the full RBS/C spectra were

recorded, only Ga-parts of the RBS/C spectra were analyzed in details, because of the higher sensitivity of the technique to heavy elements as compared to the light ones. Specifically, the Rutherford cross section is a quadratic function of the atomic number for the element involved in scattering, so the Ga signal is higher by the factor of  $\sim 15$  as compared to that of O for the same concentration.

The XRD 2theta measurements were performed using Bruker AXS D8 Discover diffractometer using Cu  $K_{\alpha 1}$  radiation in locked-coupled mode. Diffractometer is equipped with GM3 –Gobelmirror for generating high intensity parallel beam Cu  $K\alpha_{1,2}$  source and asymmetric Ge-220 double-bounce monochromater to filter Cu  $K\alpha_2$ . The diffracted beam is collected using LYNXEYE<sup>TM</sup> strip detector with 179 activated channels operated in 1-Dimensional mode (179 channels cover  $\sim 2.5^\circ$  in 2theta with resolution of  $0.014^\circ$ ). The instrument broadening is  $0.008^\circ$  for Ge (111) single crystal under the present measurement conditions with  $2.5^\circ$  soller slit in front of the LYNXEYE detector and 0.2 mm slit after the asymmetric Ge-220 double-bounce monochromater. The probing depth is  $\sim 18$  um at  $2\text{theta} = 61^\circ$  under Bragg condition.

The STEM and EELS investigations were conducted on an FEI Titan G2 60-300 kV equipped with a CEOS DCOR probe-corrector and monochromator. Observations were performed at 300 kV with a probe convergence angle of 24 mrad. The camera length was set to 60 mm and simultaneous STEM imaging was conducted with 3 detectors: high-angle annular dark field (HAADF) (collection angles 101.7-200 mrad), annular dark field (ADF) (collection angles 22.4-101.7 mrad) and annular bright field (ABF) (collection angles 8.5-22.4 mrad). The resulting spatial resolution achieved was approximately 0.08 nm. EELS was performed using a Gatan Quantum 965 imaging filter. The energy dispersion was 0.1 eV/channel and the energy resolution measured using the full width at

half maximum (FWHM) of the zero-loss peak was 1.1 eV. Electron transparent TEM samples with a cross-sectional wedge geometry were prepared by mechanical grinding and polishing (Allied MultiPrep). Final thinning was performed by Ar ion milling with a Fishione Model 1010, and plasma cleaning was applied directly before the TEM investigations, with a Fishione Model 1020.

### **First principles calculations**

The total lattice energies of the  $\text{Ga}_2\text{O}_3$  polymorphs were calculated applying density functional theory (DFT), as implemented in the VASP code [22]. The interaction between the core ( $\text{Ga}:\text{[Ar]}$  and  $\text{O}:\text{[He]}$ ) and the valence electrons were described using the projector-augmented wave (PAW) method [23]. The Perdew, Burke, and Ernzerhof (PBE) [24] gradient corrected functional was used for the exchange–correlation part of the potential for the structural optimization. The large energy cut-off of 600 eV was used to guarantee basis-set completeness. The atoms were deemed to be relaxed when all atomic forces were less than 0.02 eV  $\text{\AA}^{-1}$  and the geometries were assumed to get optimized when the total energy converged to  $\leq 1$  meV between two consecutive geometric optimization step. The crystal lattice parameters for all  $\text{Ga}_2\text{O}_3$  phases in the equilibrium were computed accordingly and the pressure was applied both isotropically and uniaxially.

### **Data availability**

All data generated or analyzed during this study are included in this article and the Supplementary Information.

### **Additional Information:**

Supplementary Information is available for this paper.

## References

1. Bernstein J., Polymorphism in Molecular Crystals. Second Edition. (Oxford University Press, 2020, pp. 608).
2. Hu, Q.Y., Shu, J.-F., Cadien, A., Meng, Y., Yang, W.G., Sheng H.W. and Mao, H.-K., Polymorphic phase transition mechanism of compressed coesite, *Nature Comm.* **6**, 6630 (2015).
3. Priolo, F. and Rimini, E., Ion-beam-induced epitaxial crystallization and amorphization in silicon, *Materials Science Reports* **5**, 321-379 (1990).
4. Debelle, A., Boulle, A., Chartier, A., Gao, F. and Weber, W. J., Interplay between atomic disorder, lattice swelling, and defect energy in ion-irradiation-induced amorphization of SiC, *Phys. Rev. B.*, **90**, 174112 (2014).
5. Sequeira, M. C., Mattei, J.-G., Vazquez, H., Djurabekova, F., Nordlund, K., Monnet, I., Mota-Santiago, P., Kluth, P., Grygiel, C., Zhang, S., Alves, E. and Lorenz, K. Unravelling the secrets of the resistance of GaN to strongly ionising radiation. *Comm. Phys.* **4**, 51 (2021).
6. Azarov, A. Yu., Hallén, A., Rauwel, P., Du, X. L., Kuznetsov, A. Yu. and Svensson, B. G., Effect of implanted species on thermal evolution of ion-induced defects in ZnO, *J. Appl. Phys.* **115**, 073512 (2014).
7. Wang, C., Yang, T., Tracy, C. L., Lu, C., Zhang, H., Hu, Y.-J., Wang, L., Qi, L., Gu, L., Huang, Q., Zhang, J., Wang, J., Xue, J., Ewing, R. C. and Wang, Y. Disorder in  $M_{n+1}AX_n$  phases at the atomic scale. *Nature Comm.* **10**, 622 (2019).
8. Anber, E. A., Foley, D., Lang, A. C., Nathaniel, J., Hart, J. L., Tadjer, M. J., Hobart, K. D., Pearton, S. and Taheri, M. L. Structural transition and recovery of Ge implanted  $\beta$ - $Ga_2O_3$ . *Appl. Phys. Lett.* **117**, 152101 (2020).

9. Playford, H. Y., Hannon, A. C., Barney, E. R. and Walton, R. I. Structures of uncharacterised polymorphs of Gallium Oxide from total neutron diffraction. *Chem.-A Eur. J.* **19**, 2803-2813 (2013).
10. Pearton, S. J., Yang, J., Cary, P. H., Ren, F., Kim, J., Tadjer, M. J. and Mastro, M. A., A review of  $\text{Ga}_2\text{O}_3$  materials, processing, and devices. *Appl. Phys. Rev.* **5**, 011301 (2018).
11. Azarov, A., Venkatachalamathy, V., Monakhov, E. V. and Kuznetsov, A. Yu. Dominating migration barrier for intrinsic defects in gallium oxide: dose-rate effect measurements. *Appl. Phys. Lett.* **118**, 232101 (2021).
12. Cora, I., Mezzadri, F., Boschi, F., Bosi, M., Čaplovičová, M., Calestani, G., Dódony, I., Pécz B. and Fornari, R. The real structure of  $\varepsilon\text{-Ga}_2\text{O}_3$  and its relation to  $\kappa$ -phase. *Cryst. Eng. Comm.* **19**, 1509 (2017).
13. Ziegler, J. F., Ziegler, M. D. and Biersack, J. P. SRIM—the stopping and range of ions in matter (2010). *Nucl. Instrum. Methods Phys. Res. B* **268**, 1818-1823 (2010).
14. Wendler, E., Treiber, E., Baldauf, J., Wolf, S. and Ronning, C., High-level damage saturation below amorphisation in ion implanted  $\beta\text{-Ga}_2\text{O}_3$ , *Nucl. Instrum. Methods Phys. Res. B* **379**, 85-90 (2016).
15. Moll, S., Zhang, Y., Debelle, A., Thomé, L., Crocombette, J. P., Zihua, Z., Jagielski, J. and Weber, W.J., Damage processes in  $\text{MgO}$  irradiated with medium-energy heavy ions, *Acta Materialia* **88**, 314–322 (2015).
16. Sharma, A., Varshney, M., Shin, H.-J., Chae, K. H., and Won, S. O. Investigation on cation distribution and luminescence in spinel phase  $\gamma\text{-Ga}_{3-\delta}\text{O}_4 : \text{Sm}$  nanostructures using X-ray absorption spectroscopy. *RSC Adv.* **7**, 52543-52554 (2017).

17. Cora, I., Fogarassy, Zs., Fornari, R., Bosi, M., Rečnik, A., and Pécz, B. *In situ* TEM study of  $\kappa \rightarrow \beta$  and  $\kappa \rightarrow \gamma$  phase transformations in  $\text{Ga}_2\text{O}_3$ . *Acta Materialia* **183**, 216-227 (2020).
18. Machon, D., McMillan, P. F., Xu, B. and Dong, J. High-pressure study of the  $\beta$ -to- $\alpha$  transition in  $\text{Ga}_2\text{O}_3$  *Phys. Rev. B* **73**, 094125 (2006).
19. M. E. Ingebrigtsen, A. Yu. Kuznetsov, B. G. Svensson, G. Alfieri, A. Mihaila, U. Badstübner, A. Perron, L. Vines, and J. B. Varley, Impact of proton irradiation on conductivity and deep level defects in  $\beta\text{-Ga}_2\text{O}_3$ , *APL Mater.* **7**, 022510 (2019).
20. Wallace, J. B., Bayu Aji, L. B., Shao, L. and Kucheyev, S. O., Deterministic role of collision cascade density in radiation defect dynamics in Si, *Phys. Rev. Lett.* **120**, 216101 (2018).
21. Feldman, L. C., Mayer, J. W. and Picraux, S. T., *Materials Analysis by ion Channeling: Submicron Crystallography* (Academic, New York, 1982)
22. Kresse, G. and Furthmüller, J. Efficient iterative schemes for *ab initio* total-energy calculations using a plane-wave basis set. *Phys. Rev. B* **54**, 11169 (1996).
23. Blöchl, P. E. Projector augmented-wave method. *Phys. Rev. B* **50**, 17953 (1994).
24. Perdew, J. P., Burke, K., and Ernzerhof, M. Generalized Gradient Approximation Made Simple. *Phys. Rev. Lett.* **77**, 3865-3868 (1996).

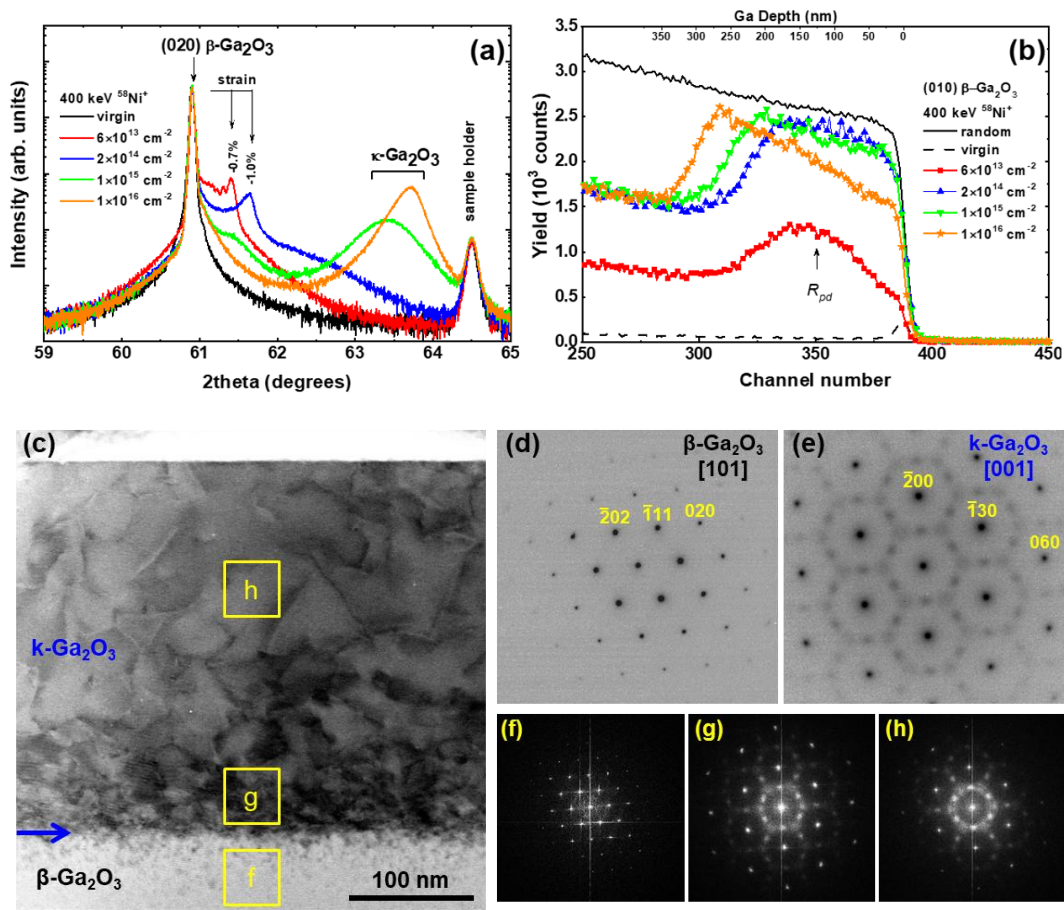


**Fig. 1** Ion-beam-induced  $\beta$ -to- $\kappa$  phase transformation in  $\text{Ga}_2\text{O}_3$ . (a) XRD 2theta scans of the samples implanted with 400 keV  $^{58}\text{Ni}^+$  ions as a function of ion dose, showing initial accumulation of the strain, followed by the appearance of the  $\kappa$ -phase related reflections at  $63\text{--}64^\circ$  angles. (b) The corresponding RBS/C spectra with the random and virgin (unimplanted) spectra shown for comparison. The maximum of nuclear energy loss profile ( $R_{pd}$ ) predicted with SRIM code [13] simulations is shown in correlation with the depth scale. (c) ABF-STEM image of  $\beta\text{-Ga}_2\text{O}_3$  sample irradiated with  $1\times 10^{16}$   $\text{Ni}/\text{cm}^2$ . Panels (d) and (e) illustrate SAED patterns from the unimplanted and implanted regions respectively; (f-h) FFTs from high-resolution images taken from different regions of the sample as indicated in the panel (c).

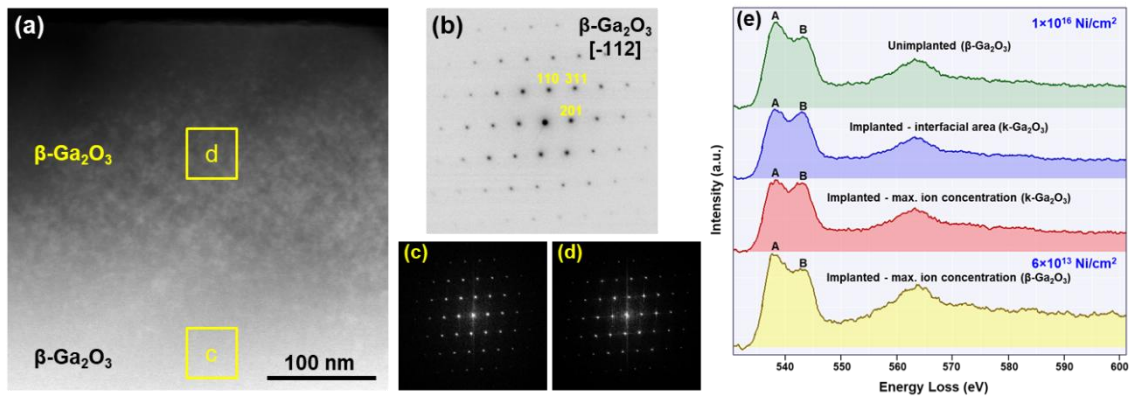


**Fig. 2 Microstructure of the low-dose implanted  $\beta$ - $\text{Ga}_2\text{O}_3$  sample and EELS spectra of  $\beta$ - and  $\kappa$ -phases.** (a) ADF-STEM image of  $\beta$ - $\text{Ga}_2\text{O}_3$  sample implanted with  $6 \times 10^{13}$   $\text{Ni}/\text{cm}^2$ , (b) corresponding SAED pattern at the depth of  $R_{pd}$  and (c)-(d) FFTs from high-resolution images taken from the unimplanted and implanted regions, respectively. Panel (e) shows EELS spectra of the oxygen-K edge, acquired from different areas of the high-dose and low-dose implanted  $\beta$ - $\text{Ga}_2\text{O}_3$ , illustrating characteristic intensity changes correlated with  $\beta$ -to- $\kappa$  transition.

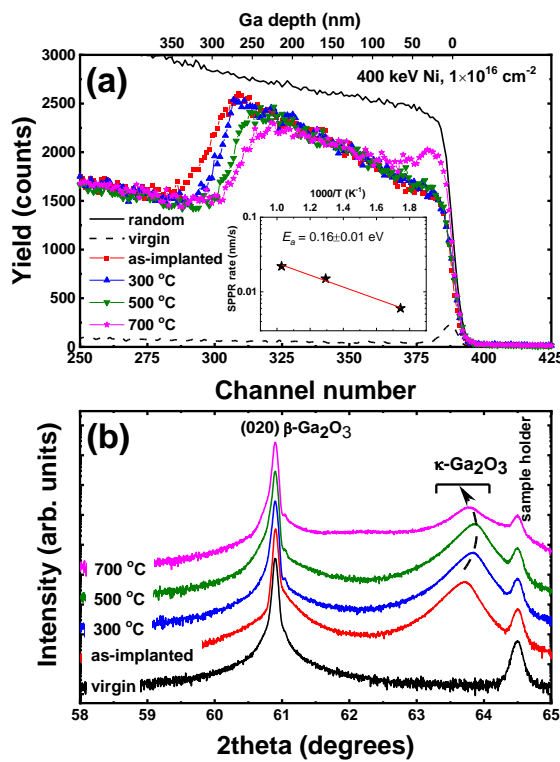


**Fig. 3 Thermal stability of the ion-beam-induced  $\kappa$ -Ga<sub>2</sub>O<sub>3</sub> film.** (a) RBS/C spectra and (b) corresponding XRD 2theta scans of the sample shown in Fig. 1(c) before and after isochronal anneals as indicated in the legend. The inset in the panel (a) shows Arrhenius plot of the solid-phase polymorphic regrowth rate as deduced from the RBS/C data.

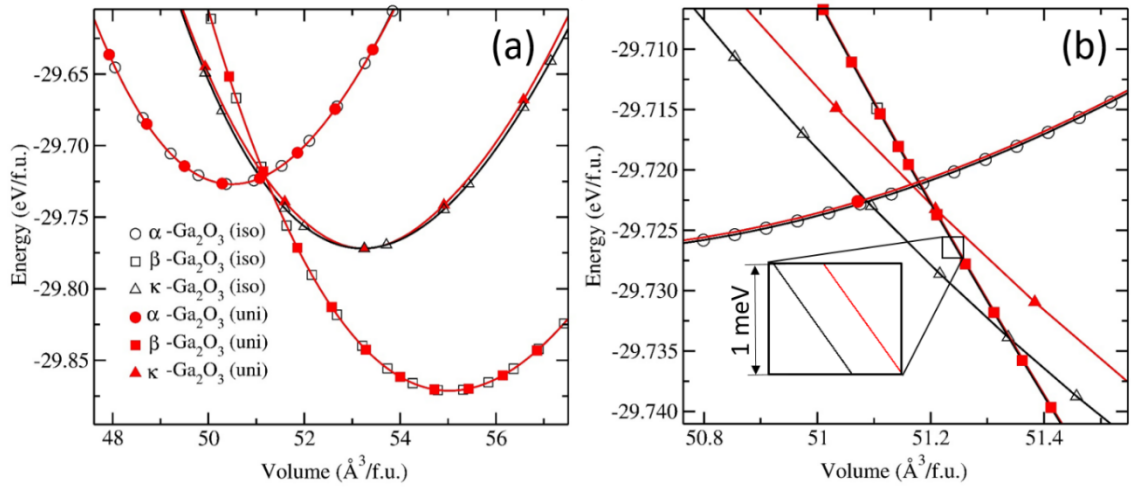


**Fig. 4. DFT calculated lattice energies for  $\alpha$ -,  $\beta$ -, and  $\kappa$ - $\text{Ga}_2\text{O}_3$  as a function of the volume per formula unit for (a) bigger interval showing energy minima for the corresponding phases and (b) smaller interval emphasizing the transition points. The data were collected under isotropic (open symbols) and uniaxial stress along [010] direction (filled symbols). As seen from panel (b), the energy difference while applying the isotropic and uniaxial stress is significant for  $\kappa$ - $\text{Ga}_2\text{O}_3$ , but negligible for  $\alpha$ - and  $\beta$ -phases as highlighted in the inset in panel (b).**

Supplementary materials for  
Disorder-induced ordering in gallium oxide polymorphs

Alexander Azarov<sup>1,a)</sup>, Calliope Bazioti<sup>1</sup>, Vishnukanthan Venkatachalamapathy<sup>1,2</sup>,  
Ponniah Vajeeston<sup>3</sup>, Edouard Monakhov<sup>1</sup>, and Andrej Kuznetsov<sup>1, b)</sup>

<sup>1)</sup> *University of Oslo, Department of Physics, Centre for Materials Science and Nanotechnology, PO Box 1048 Blindern, N-0316 Oslo, Norway*

<sup>2)</sup> *Department of Materials Science, National Research Nuclear University, “MEPhI”, 31 Kashirskoe Hwy, 115409 Moscow, Russian Federation*

<sup>3)</sup> *University of Oslo, Department of Chemistry, Centre for Materials Science and Nanotechnology, PO Box 1033 Blindern, N-0315 Oslo, Norway*

<sup>a)</sup> [alexander.azarov@smn.uio.no](mailto:alexander.azarov@smn.uio.no)

<sup>b)</sup> [andrej.kuznetsov@fys.uio.no](mailto:andrej.kuznetsov@fys.uio.no)

## Section I. Identification of the $\kappa$ -phase XRD peaks and anisotropy effects

Figure S1 shows 2theta scans of the (010) oriented  $\beta$ - $\text{Ga}_2\text{O}_3$  crystals implanted with Ni and Au ions in comparison with the virgin sample. Accounting for the SAED pattern in Fig. 1(e), the peak at  $63.76^\circ$  in the sample implanted with  $1 \times 10^{16} \text{ Ni/cm}^2$  can be unambiguously identified; it is associated with the diffraction from the {010} family of planes and specifically (060) planes in  $\kappa$ -phase, see the corresponding dashed line label in Fig. S1. Notably, other signatures of the {010} planes were not observed, attributed to the structure factor exclusions.

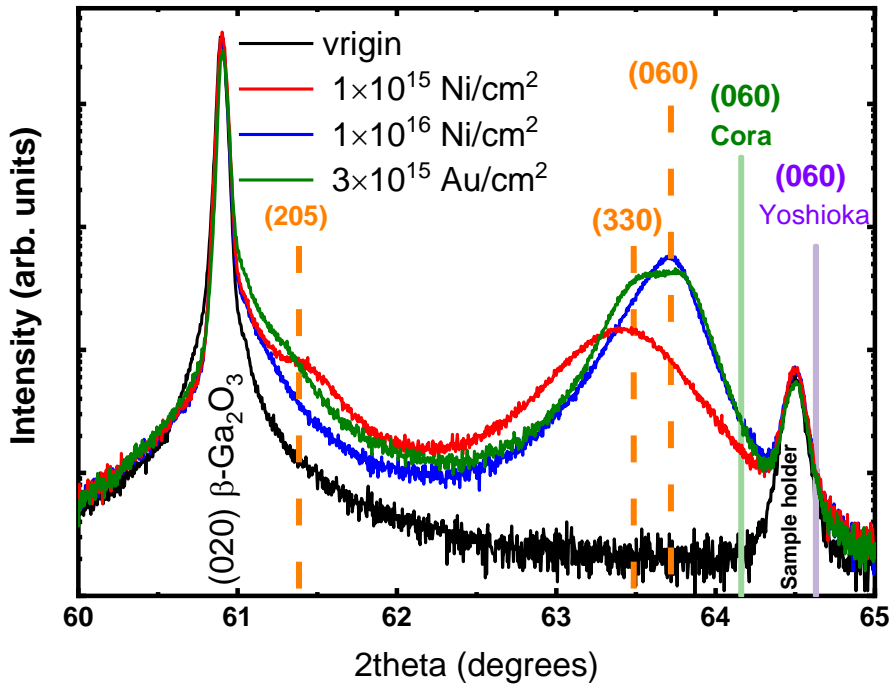


**Fig. S1** XRD 2theta scans of the (010) oriented  $\beta$ - $\text{Ga}_2\text{O}_3$  crystals implanted with  $1 \times 10^{15} \text{ Ni/cm}^2$ ,  $1 \times 10^{16} \text{ Ni/cm}^2$  and  $3 \times 10^{15} \text{ Au/cm}^2$ . The scan of the virgin  $\beta$ - $\text{Ga}_2\text{O}_3$  crystal is also included for comparison. Continuous and dashed lines label diffraction positions based on the literature [SR1, SR2] and the present analysis, respectively.

Notably,  $63.76^\circ$  for the  $\kappa$ -phase (060) diffraction is  $\sim 0.5^\circ$  and  $1^\circ$  lower comparing with the data reported by Cora et al [SR1] and by Yoshioka et al [SR2], respectively, as also

labelled by the corresponding continuous lines in Fig. S1. Converting the angular position to the interplanar distance, we obtain 0.1459 nm in comparison with 0.1450 nm by Cora et al [SR1]. Considering that 0.1450 nm characterizes the relaxed lattice, our data indicate +0.62% strained lattice, assuming isotropic strain. In the following, we will account for this order of strain as a correction factor while identifying other peaks.

The sample implanted with  $3 \times 10^{15}$  Au/cm<sup>2</sup> was designed to mimic the ballistic defect production rates for that in  $1 \times 10^{16}$  Ni/cm<sup>2</sup> and as such was expected to result into similar phase transformation. However, for this sample, a double peak centered at 63.52° and 63.76° is observed, see Fig. S1. The 63.76° peak can be readily assigned to the  $\kappa$ -phase (060) diffraction as discussed above, while the 63.52° peak can be associated with  $\kappa$ -phase (330) planes shifted from Cora et al data [SR1] by the strain factor of +0.61 %. Further, in the sample implanted with  $1 \times 10^{15}$  Ni/cm<sup>2</sup>, the (060) diffraction is missing, however the (330) related diffraction is still observed, even though it is centered at 63.43° - see Fig. S1 – consistently with the strain factor correction of +0.72 %. Altogether it suggests a very interesting dynamics of the  $\beta$ -to- $\kappa$  phase transformation upon the accumulation of the radiation induced lattice disorder; exhibiting a balance in terms of the preferential orientation(s) as a function of the disorder accumulation. Indeed, the difference between  $3 \times 10^{15}$  Au/cm<sup>2</sup> and  $1 \times 10^{16}$  Ni/cm<sup>2</sup> implants may be attributed to the non-linear cascade density effects [SR3] for ions with significantly different masses (see also Supplementary Materials III). Lastly, in respect with Fig. S1, there is an additional peak, centered at 61.33° and most clearly seen in the sample implanted with  $1 \times 10^{15}$  Ni/cm<sup>2</sup>. This peak is attributed to the  $\kappa$ -phase (205) planes with the strain factor correction of +0.72 % in respect with Cora et al data [SR1]. Notably, the analysis above excludes contributions from planes belonging to other Ga<sub>2</sub>O<sub>3</sub> polymorphs; primarily because we know from STEM that single  $\kappa$ -phase forms and additionally because all other polymorphs are higher

in energy. In fact, considering the energetic aspects (see Supplementary Materials - IV), the only additional realistic option is to add  $\alpha$ -phase into considerations here, but as we showed it above, the data in Fig. S1 are explainable in terms  $\kappa$ -phase only.

The implants done into (-201) oriented  $\beta$ - $\text{Ga}_2\text{O}_3$  crystals confirm the general character of the phenomena. Indeed, Fig. S2 shows XRD-2theta scans of the (-201) oriented  $\beta$ - $\text{Ga}_2\text{O}_3$  crystals implanted with  $\text{Ni}^+$  ions (a) (-402) diffraction centered at  $38.38^\circ$  and (b) (-603) diffraction centered at  $59.08^\circ$ . For the low dose implant, the shoulder peak forms at the low-angle side of both (-402) and (-603) reflections. Notably, these shoulder peaks comprise the well-defined fringes, with increasing number of fringes from (-402) to (-603) reflections. This observation resembles that in Fig. 1(a), however the planes in  $\beta$ - $\text{Ga}_2\text{O}_3$  in Fig. S2 are subjected to the tensile strain. Meanwhile, similarly to that in Fig. 1(a), for the highest dose ( $1 \times 10^{16}$   $\text{Ni}/\text{cm}^2$ ), the strain is released and the new polymorph formation is observed with a double peak in Fig. S2(a) centered at  $37.75^\circ$  and  $36.67^\circ$ . In the first approximation, neglecting the anisotropy effects, the same implantation dose might produce the same radiation-induced disorder, in its turn resulting into the same  $\beta$ -to- $\kappa$  phase transformation in both (010) and (-201) oriented  $\beta$ - $\text{Ga}_2\text{O}_3$  crystals. However, evidently, the anisotropy plays a role, resulting in a double XRD peak in Fig. S2(a) explainable either in terms of the double orientation or double phase. Also very interestingly,  $2 \times 10^{14}$   $\text{Ni}/\text{cm}^2$  implants were still associated with the strain accumulation in the (010) oriented  $\beta$ - $\text{Ga}_2\text{O}_3$  – see Fig. 1(a); however, distinct diffraction peak at  $36.67^\circ$  forms for the same implantation conditions in (-201) oriented  $\beta$ - $\text{Ga}_2\text{O}_3$  – see Fig. S2(a), confirming the importance of the anisotropy effects. Nevertheless, qualitatively, the trend for  $\beta$ -to- $\kappa$  transformation holds. Applying 1.75% compressive strain correction for the planes positions from literature [SR1], we may label (201), (131) and (210)  $\kappa$ -phase planes at  $36.88^\circ$ ,  $37.00^\circ$ , and  $37.07^\circ$ , respectively, see Fig. S2. Notably, there could be

alternative identification scenarios for peaks in Fig. S2(a) proposed in terms of other polymorphs too; e.g.  $\varepsilon$ -Ga<sub>2</sub>O<sub>3</sub>,  $\gamma$ -Ga<sub>2</sub>O<sub>3</sub> and  $\delta$ -Ga<sub>2</sub>O<sub>3</sub> exhibit peaks centered at 37.14°, 37.27° and 38.28° associated with (101), (222) and (332) planes, respectively. However, as mentioned above, these options were excluded from the consideration, because of the STEM observation and the energetic reasons.

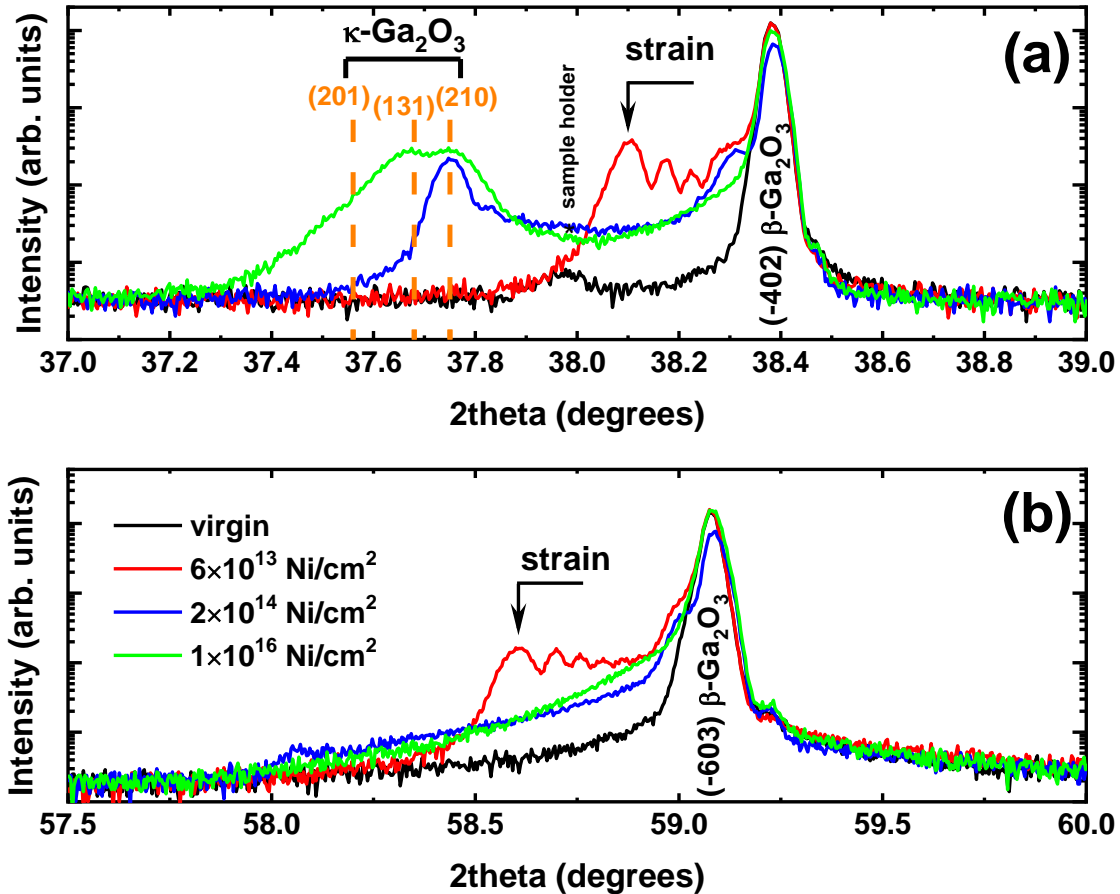


**Fig. S2** XRD 2theta scans across (-402) and (-603) reflections of the (-201) oriented  $\beta$ -Ga<sub>2</sub>O<sub>3</sub> crystals implanted with Ni<sup>+</sup> ions as indicated in the legend. Dashed lines label the  $\kappa$ -Ga<sub>2</sub>O<sub>3</sub> planes responsible for the diffraction based on present analysis.

Notably, no new phase-related peaks appear in Fig. S2(b) around (-603) reflection of  $\beta$ -Ga<sub>2</sub>O<sub>3</sub>. The broader background observed for (-603) reflection of  $\beta$ -Ga<sub>2</sub>O<sub>3</sub> may be attributed to the extended defects or lattice distortions [SR4].

## Section II. Analysis of the adjacent $\kappa$ -phase grains exhibiting different strain contrast.

Even though the film in Fig. 1(c) was clearly interpreted as single  $\kappa$ -phase film, there are still remaining questions, in particular related to potential mis-orientation between the grains as well as regarding potential chemical variations. For that reason, we investigated two adjacent grains in Fig. S3. As seen from Fig. S3, the grains are nicely co-oriented and there are no chemical inhomogeneities observed.

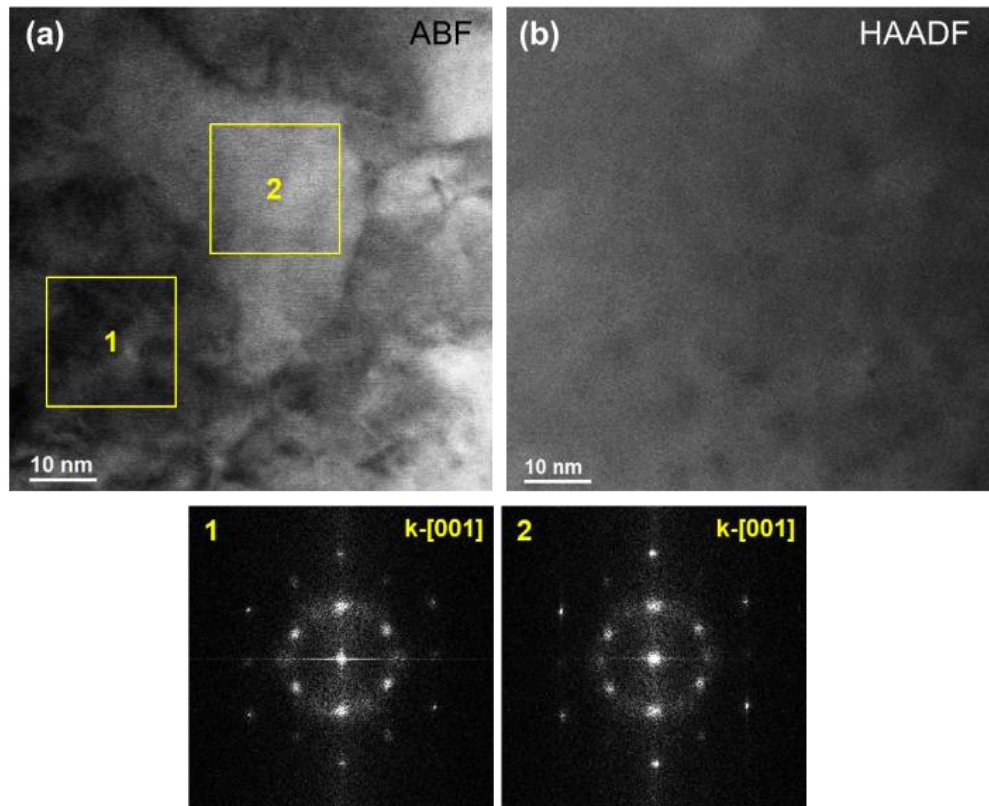


**Fig. S3** (a) ABF-STEM and (b) HAADF-STEM high-resolution images acquired simultaneously from the maximum ion-concentration region of (010)  $\beta$ -Ga<sub>2</sub>O<sub>3</sub> irradiated with  $1 \times 10^{16}$  Ni/cm<sup>2</sup>. FFTs extracted from two adjacent grains reveal that both grains are stabilized in  $\kappa$ -phase and have the same orientation. The stable contrast in HAADF (pure Z-contrast image) indicates no chemical variations and the contrast in ABF is attributed only to the strain.

### Section III. Implants with different ions normalized to produce similar number of atomic displacements

In the main part of the paper we selected to show the data for systematic  $^{58}\text{Ni}^+$  ion implants, however  $^{69}\text{Ga}^+$ , and  $^{197}\text{Au}^+$  implants data were systematically exploited too, and used for comparison to demonstrate the general character of the phenomena (as already shown in Fig. S1 in Supplementary Materials – I). For that reason, the ballistic defect production rates (without accounting for non-linear cascade density effects [SR3]) for  $^{69}\text{Ga}^+$ , and  $^{197}\text{Au}^+$  implants were normalized to that of  $^{58}\text{Ni}^+$  ion implanted with 400 keV in a wide dose range of  $6 \times 10^{13}$  -  $1 \times 10^{16}$  cm $^{-2}$ . Specifically, we used SRIM code [SR5] simulations to choose roughly similar profiles of the primary defects or displacements per atom (DPA). In these calculations, displacement energies of 25 and 28 eV were used for Ga and O atoms, respectively. Fig. S4 provides a representative example of the corresponding RBS/C and XRD data, while the inset in Fig. S4(a) showing the DPA depth profiles of DPA for Ni, Ga and Au implants. As seen from Fig. S4, both the RBS/C profiles and XRD 2theta scans exhibit very similar trends for the all ion species used. Thus, the observed polymorph transitions are attributed to the disorder-induced effects with negligible impact of the chemical nature of the ions. Notably, Au ions produced the thickest modified layer, as seen from Fig. S4(a), despite that the corresponding DPA profile is most shallow, see the inset in Fig. S4(a). This effect is readily explainable in terms of variations in the cascade density effects [SR3] not taken in account by SRIM.

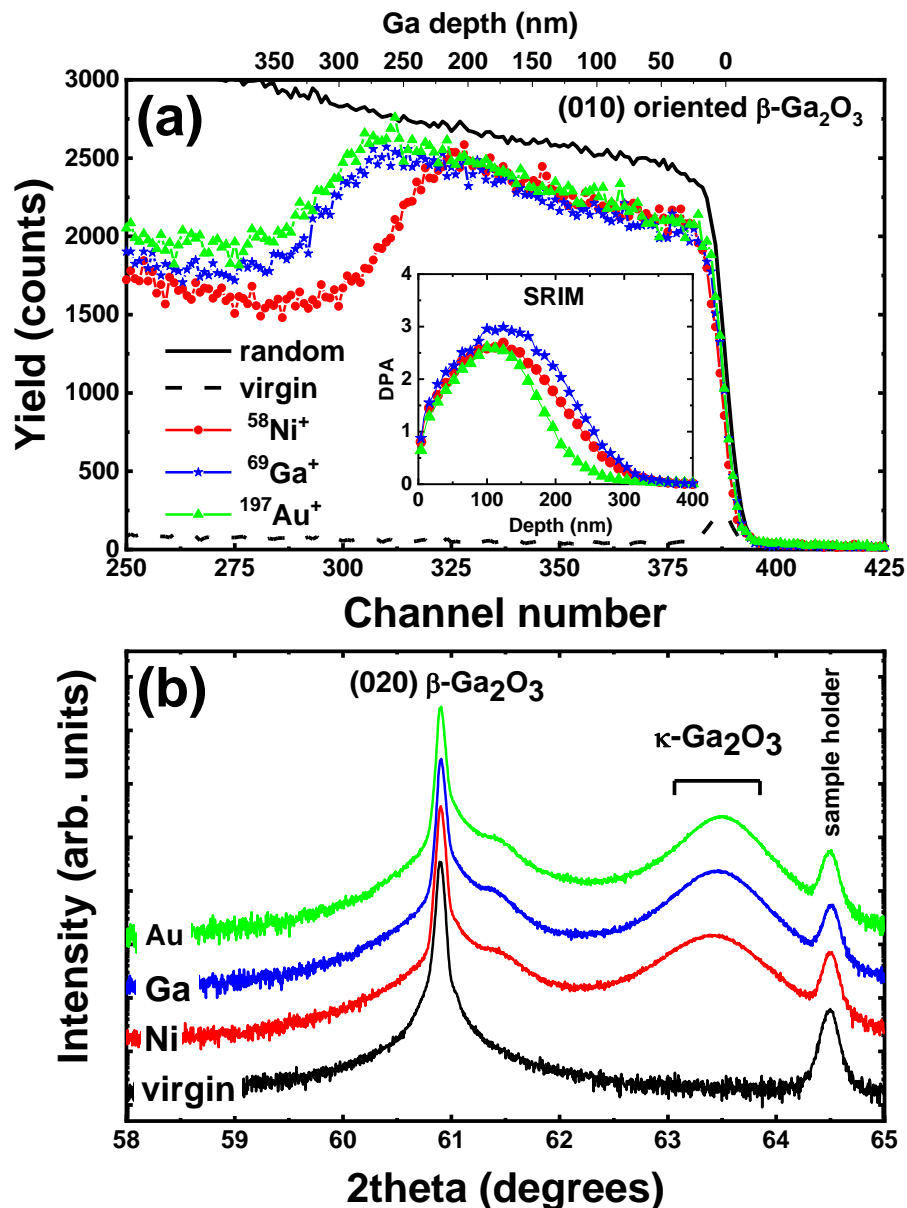


**Fig. S4** (a) RBS/C spectra and (b) XRD 2theta scans of the (010) oriented  $\beta$ -Ga<sub>2</sub>O<sub>3</sub> crystals implanted with 400 keV  $^{58}\text{Ni}^+$  ( $1 \times 10^{15} \text{ cm}^{-2}$ ), 500 keV  $^{69}\text{Ga}^+$  ( $1 \times 10^{15} \text{ cm}^{-2}$ ) and 1.2 MeV  $^{197}\text{Au}^+$  ions ( $3 \times 10^{14} \text{ cm}^{-2}$ ). The inset in the panel (a) shows the depth profiles of displacements per atom (DPA) as generated by Ni, Ga and Au ions ion impacts, as simulated by the SRIM code [SR5].

#### Section IV. $\text{Ga}_2\text{O}_3$ polymorphs equilibrium and pressure induced transformations

In the present work, we consider six experimentally determined polymorphs ( $\alpha$ ,  $\beta$ ,  $\kappa$ ,  $\delta$ ,  $\gamma$  and  $\varepsilon$ ) of  $\text{Ga}_2\text{O}_3$  and Fig. S5 summarizes calculated the total energy vs volume per formula unit for these  $\text{Ga}_2\text{O}_3$  polymorphs applying DFT.

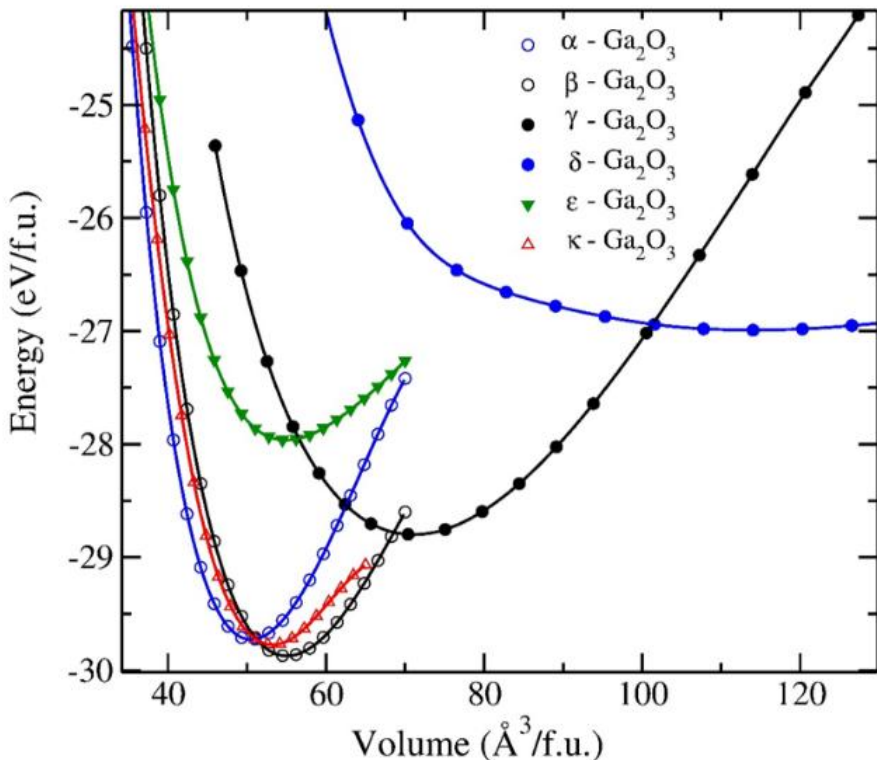


**Fig. S5** Lattice total energy vs volume per formula unit for six different  $\text{Ga}_2\text{O}_3$  polymorphs obtained with DFT calculations.

The frozen phonon calculation was performed on these polymorphs using the Phonopy program to obtain the phonon dispersion curve and the density of states (DOS) [SR6]. An atomic displacement of 0.0075 Å was used, with a symmetry consideration, to obtain the force constants for the phonon calculations. The displacements in opposite directions along all axes were incorporated in the calculations to improve the overall precision. The force calculations were made using the VASP code with the supercell approach and the resulting data were imported into the Phonopy program. The dynamical matrices were

calculated from the force constants, and phonon DOS curves were computed using the Monkhorst-Pack scheme [SR7]. As an example, Fig. S6 shows the calculated total phonon DOS for  $\alpha$ -,  $\beta$ -, and  $\kappa$ -polymorphs confirming their dynamic stability.

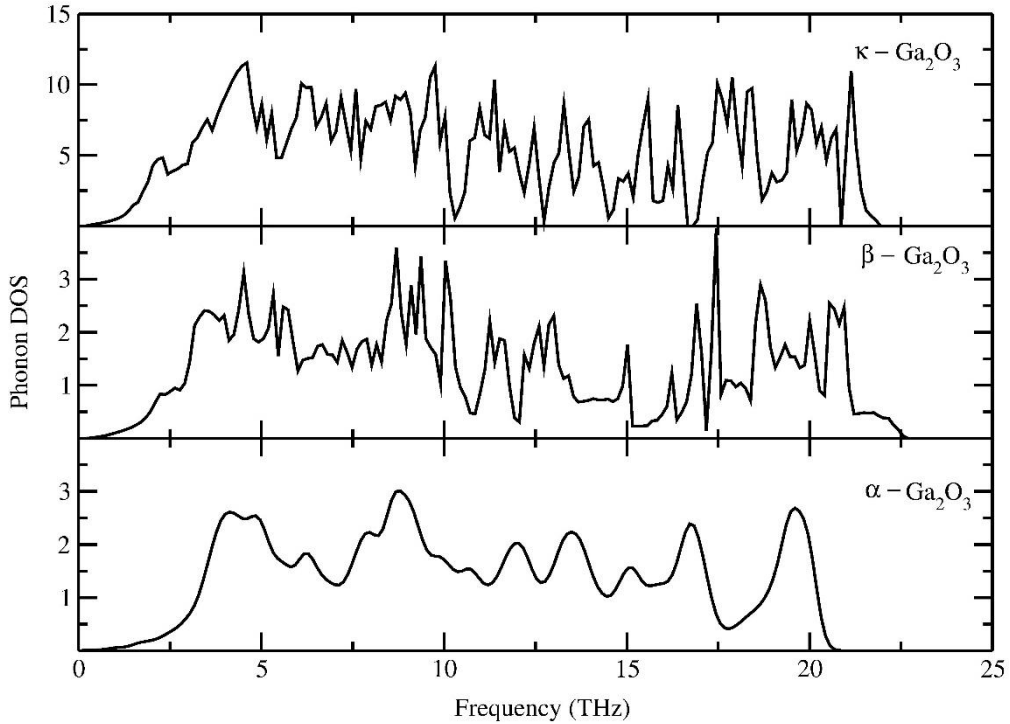


**Fig. S6** Calculated phonon density of states for  $\alpha$ -,  $\beta$ -, and  $\kappa$ -polymorphs of  $\text{Ga}_2\text{O}_3$  at 0 GPa pressure and 0 K temperature.

Further, the effect of the applied external pressure was investigated for  $\alpha$ -,  $\beta$ -, and  $\kappa$ -polymorphs and Fig. S7 illustrate the situation setting the Gibbs energy of the  $\beta$ -phase to zero. Fig. S7 reveals that the  $\beta$ - to  $\kappa$  phase transition occurs at the range of 9.8 - 13.4 GPa accounting for the isotropic pressure. This is in agreement with the observation of the  $\beta$ -to- $\alpha$  phase transition for pressures exceeding 13.6 GPa [SR8]. Importantly, the actual energy difference between  $\alpha$ -,  $\beta$ -, and  $\kappa$ -polymorphs is fairly small – as illustrated by Fig. 4 in the main part of the paper – providing an opportunity for the structure to remain in the metastable form even after the pressure release. Notably, the application of the isotropic pressure may be regarded as naïve. Indeed,  $\beta$ -  $\text{Ga}_2\text{O}_3$  has the compressibility for the  $a$ ,  $b$ , and  $c$  lattice-parameters of 6.0, 3.7, and 4.2 %, respectively, and  $\beta$ -angle increased by

1.9%;  $\alpha$ -  $\text{Ga}_2\text{O}_3$  had the compressibility of the  $a$  and  $c$  lattice-parameters of 3.3 and 7.1 %, respectively [SR9]. In practice, different “threshold” pressures for  $\text{Ga}_2\text{O}_3$  polymorph transitions were reported experimentally [SR10]. In our data, we also noticed that different levels of disorder, and subsequently of strain, are required for igniting the  $\beta$ - to  $\kappa$  phase transition in differently oriented  $\beta$ -  $\text{Ga}_2\text{O}_3$  crystals (see e.g. Figs. S1 - S2). Thus, we have also tested the application of the uniaxial pressure as shown in Fig. 4 in the main text of the paper.

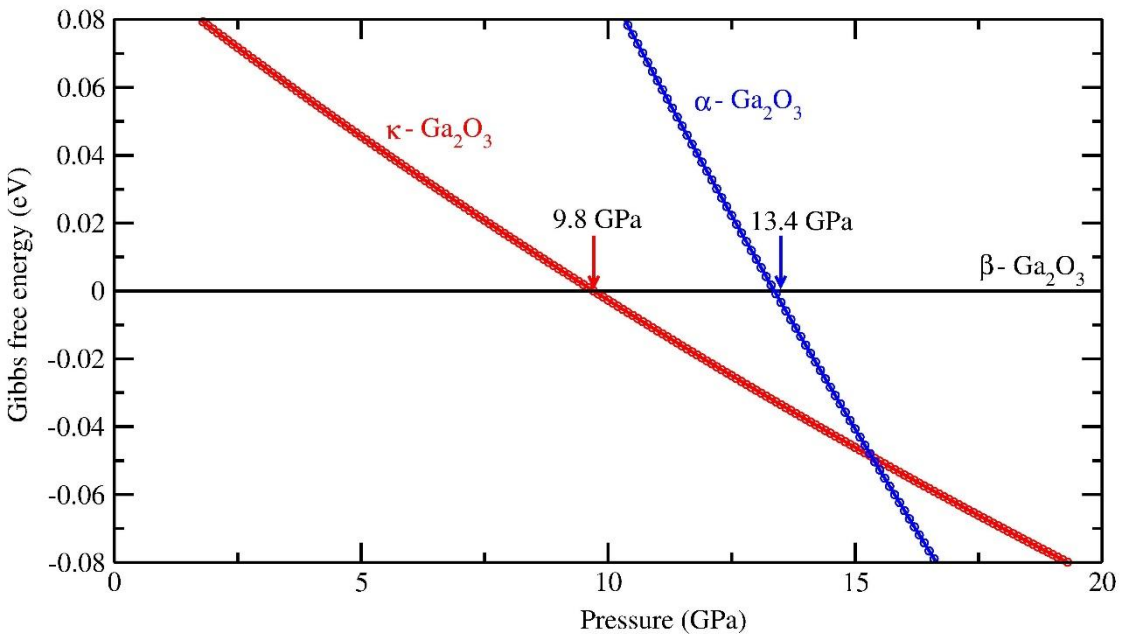


**Fig. S7** Stability of  $\kappa$  and  $\alpha$ - $\text{Ga}_2\text{O}_3$  polymorphs relative to  $\beta$ - $\text{Ga}_2\text{O}_3$  as a function of the isotropic pressure. The transition pressures are marked by arrows at the corresponding transition points.

In addition to the anisotropic effects, temperature can have a decisive role in controlling the direction of the metastable strain-induced polymorph transitions. One can account for temperature effects using the Gibbs free energy  $G(T, p) = E^{\text{tot}} + F^{\text{vib}} - TS^{\text{conf}} + pV$ .

Where, the total energy  $E^{\text{tot}}$ , essentially plotted in Fig. S5; vibrational free energy,  $F^{\text{vib}}$  accounts for the vibrational contributions with  $F^{\text{vib}} = E^{\text{ZPE}} - TS^{\text{vib}}$ ;  $TS^{\text{conf}}$  includes configurational entropy; and  $pV$  is the pressure-volume factor. Fig. S8 shows the free

energy for  $\beta$ -,  $\alpha$ - and  $\kappa$ -polymorphs as a function of temperature at 0 and 10 GPa pressures, showing that the temperature variations will obviously increase the complexity; however, potentially leading to an additional flexibility to obtain single-phase  $\kappa$ - $\text{Ga}_2\text{O}_3$ , instead of the  $\kappa/\alpha$  mixture. Indeed, as seen from Fig. S8, the energy difference between  $\alpha$ - and  $\kappa$ -phases increases with increasing temperature for the sample subjected to pressure. This effect is evident already at room temperature and extends through the whole  $\kappa$ -phase stability region as we observed it in Fig. 3 in the main part of the paper.

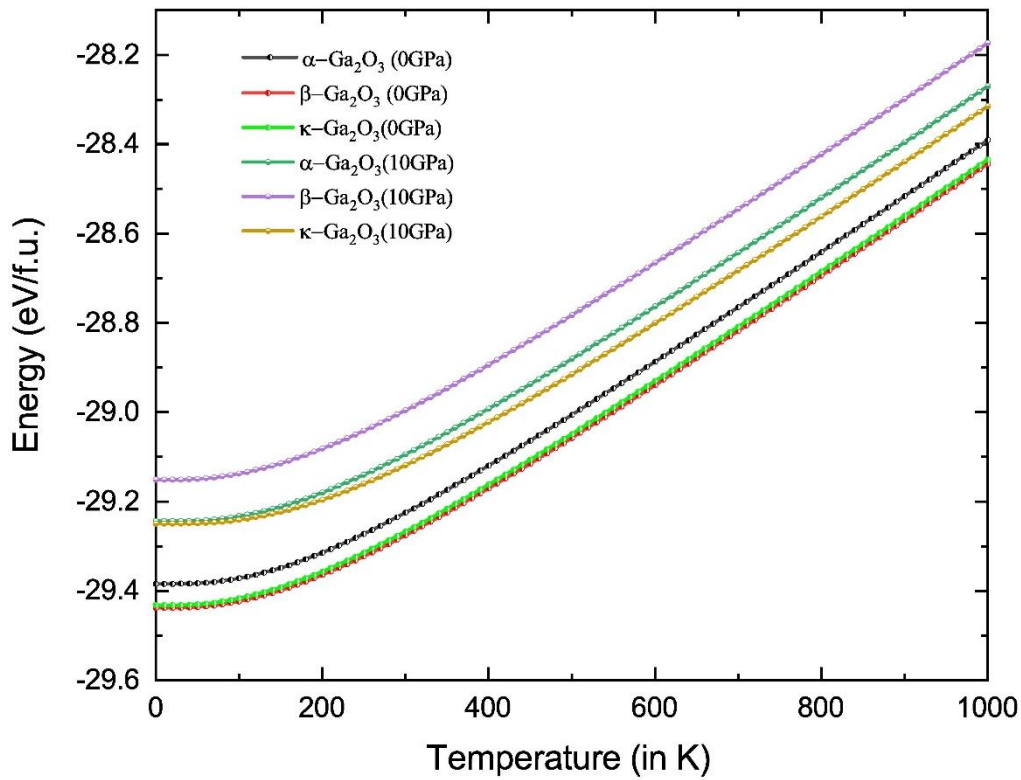


**Fig. S8** Calculated Gibbs free energy for  $\text{Ga}_2\text{O}_3$  polymorphs as a function of temperature 0 GPa and at 10 GPa.

## Section V. Effect of the implantation temperature

As predicted by Fig. S8, the energy difference between  $\alpha$ - and  $\kappa$ -phases increases with increasing temperature for the sample subjected to pressure. However, temperature might also affect the balance between out-diffusion and annihilation of the radiation-induced defects, making it to an important factor for the localization of the  $\beta/\kappa$  interface in respect

with the  $R_{pd}$  region, as illustrated in Fig. S9. As seen from Fig. S9(a), the film thickness shrinks as a function of the implantation temperature, while Fig. S9(b) confirms the maintenance of the  $\kappa$ -phase XRD-peaks, evolving to a double-peak for the 300 °C implant.

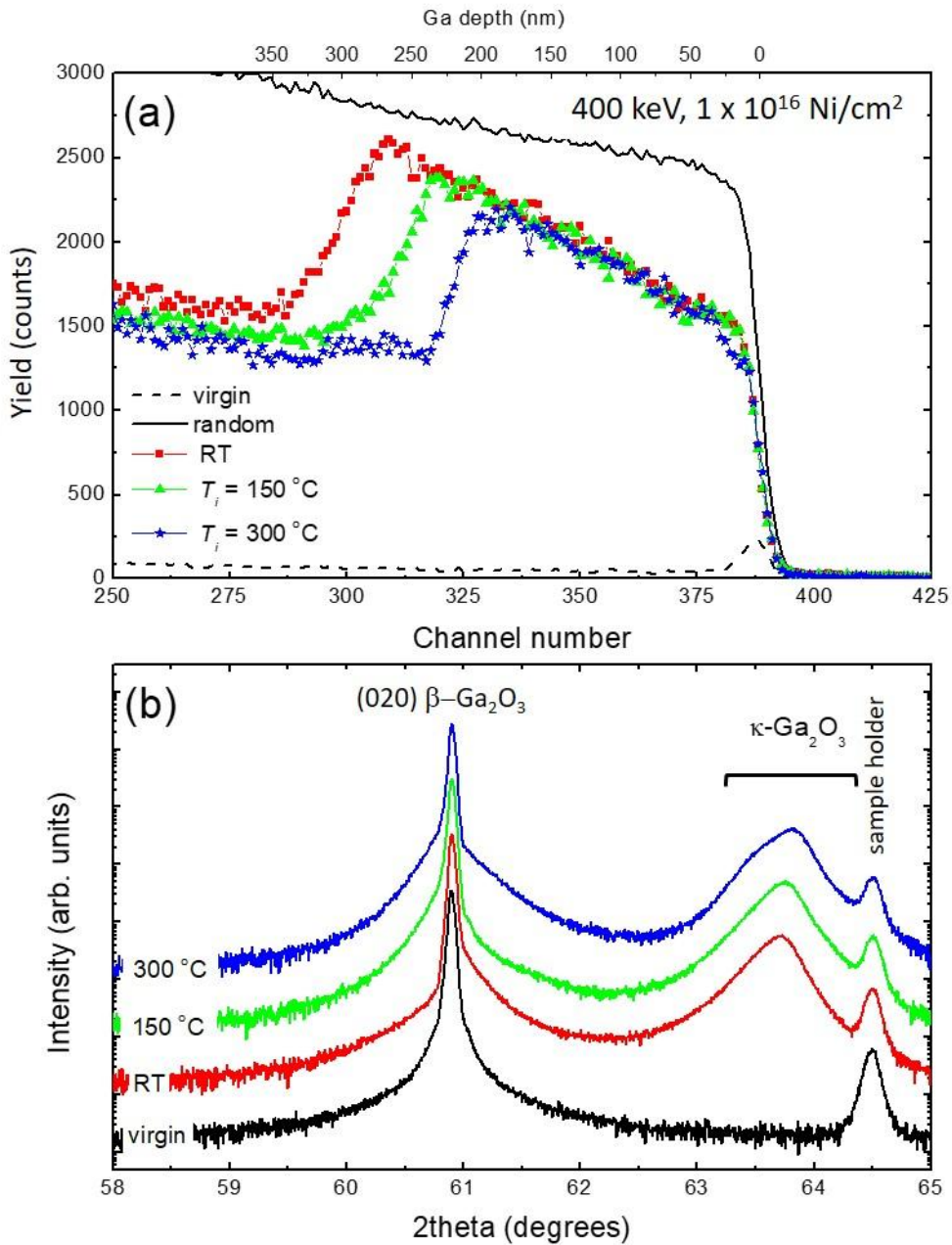


**Fig. S9** (a) RBS/C spectra and (b) XRD 2theta scans of the (010) oriented  $\beta$ -Ga<sub>2</sub>O<sub>3</sub> crystals implanted with 400 keV,  $1 \times 10^{16}$  Ni/cm<sup>2</sup> at different temperatures as indicated in the legend. The data for the room temperature (RT) implant are the same as in Figs.1 and 3.

References:

- SR1. Cora, I., Mezzadri, F., Boschi, F., Bosi, M., Čaplovičová, M., Calestani, G., Dódony, I., Pécz B. and Fornari, R. The real structure of  $\varepsilon$ -Ga<sub>2</sub>O<sub>3</sub> and its relation to  $\kappa$ -phase. *Cryst. Eng. Comm.* **19**, 1509 (2017).
- SR2. Yoshioka, S., Hayashi, H., Kuwabara, A., Oba, F., Matsunaga, K., and Tanaka, I. Structures and energetics of Ga<sub>2</sub>O<sub>3</sub> polymorphs. *J. Phys.: Condens. Matter* **19** (2007) 346211
- SR3. Wallace, J. B., Bayu Aji, L. B., Shao, L. and Kucheyev, S. O., Deterministic role of collision cascade density in radiation defect dynamics in Si, *Phys. Rev. Lett.* **120**, 216101 (2018).
- SR4. Wendler, E., Treiber, E., Baldauf, J., Wolf, S., and Ronning, C. High-level damage saturation below amorphisation in ion implanted  $\beta$ -Ga<sub>2</sub>O<sub>3</sub>. *Nucl. Instrum. Methods Phys. Res. B* **379**, 85 (2016).
- SR5. Ziegler, J. F., Ziegler, M. D. and Biersack, J. P. SRIM—the stopping and range of ions in matter (2010), *Nucl. Instrum. Methods Phys. Res. B* **268**, 1818 (2010).
- SR6. Togo, A., Oba, F., and Tanaka, I. First-principles calculations of the ferroelastic transition between rutile-type and CaCl<sub>2</sub>-type SiO<sub>2</sub> at high pressures, *Phys. Rev. B* **78**, 134106 (2008).
- SR7. Monkhorst, H.J., and Pack, J. D. Special points for Brillouin-zone integrations, *Phys. Rev. B* **13**, 5188 (1976).
- SR8. Wang, H., He, Y., Chen, W., Zeng, Y. W., Stahl, K., Kikegawa, T., Jiang, J. Z. High-pressure behavior of  $\beta$ -Ga<sub>2</sub>O<sub>3</sub> nanocrystals. *J. Appl. Phys.* **107**, 033520 (2010)
- SR9. Lipinska-Kalita, K. E., Kalita, P. E., Hemmers, O. A. and Hartmann, T. Equation of state of gallium oxide to 70 GPa: Comparison of quasihydrostatic and nonhydrostatic compression. *Phys. Rev. B* **77**, 094123 (2008).
- SR10. Macho, D., McMillan, P.F., Xu, B., and Dong, J. High-pressure study of the  $\beta$ -to- $\alpha$  transition in Ga<sub>2</sub>O<sub>3</sub>. *Phys. Rev. B* **73**, 094125 (2006);